Culture of primary rat hippocampal neurons: design, analysis, and optimization of a microfluidic device for cell seeding, coherent growth, and solute delivery

**Alexander C. Barbati · Cheng Fang ·
Gary A. Banker · Brian J. Kirby**

Abstract We present the design, analysis, construction, and culture results of a microfluidic device for the segregation and chemical stimulation of primary rat hippocampal neurons. Our device is designed to achieve spatio-temporal solute delivery to discrete sections of neurons with mitigated mechanical stress. We implement a geometric guidance technique to direct axonal processes of the neurons into specific areas of the device to achieve solute segregation along routed cells. Using physicochemical modeling, we predict flows, concentration profiles, and mechanical stresses within pertiment sections of the device. We demonstrate cell viability and growth within the closed device over a period of 11 days. Additionally, our modeling methodology may be generalized and applied to other device geometries.

1 Introduction

Neurobiological systems are immensely intricate and complex: exhibiting vastness in extent, variety, and connectivity. Analyses of these systems under well-constrained user-defined conditions is necessary to extract mechanisms of disease, and to develop and screen targeted therapies for acute and chronic diseases. Interrogation of these systems performed at the single- and multi-cell level enables relevant extracellular cell-scale change and control. Micro- and nanofluidic technologies, developed over the past few decades (Squires and Quake 2005; Schoch et al. 2008), are uniquely suited to extract information at the cell level (Pearce and Williams 2007), as these technologies provide devices with length scales comparable to the length scales of the cell(s) under analysis.

Although micro- and nanofluidic systems demonstrate many advantages over traditional techniques, a variety of challenges remain in the design and fabrication of these devices before neurobiological questions can be answered. Most importantly, neurons are extremely sensitive to chemical and mechanical changes in their environment. Mechanical and chemical effects can be mitigated or eliminated at the design stage by considering the bio- and physicochemical implications of the design.

Here, we present, analyze, construct, and qualify a novel microfluidic device to deliver soluble factors to specific locations on an array of coherently grown rat hippocampal neurons with temporal control. Our device improves on the current state-of-the-art by providing for both coherent arrays of neurons in concert with a delivery scheme providing spatial and temporal control of solutes at specific locations along the axon of the cell, while leaving the cell soma undisturbed. Furthermore, our device design approach stresses well-characterized mass and momentum transport to enable neurobiological experiments.

A. C. Barbati · B. J. Kirby (✉)
Sibley School of Mechanical and Aerospace Engineering, Cornell University, Ithaca, NY, USA
e-mail: kirby@cornell.edu

C. Fang · G. A. Banker
Jungers Center for Neurosciences Research, Oregon Health and Sciences University, Portland, OR, USA

Deficiencies of the intracellular transport mechanism in neurobiological systems are putative causes of neurobiological damage and disease (De Vos et al. 2008). The biological transport mechanism within the neuron may fail at several levels with the same result. Cargo-carrying molecular motors, energy-producing mitochondria, microtubules (upon which the molecular motors move), and the mechanism of cargo attachment are all susceptible to damage resulting in transport breakdown and cell damage or death (De Vos et al. 2008). Species such as sodium azide (Selvatici et al. 2009) (NaN_3) and peroxynitrite (Szabo et al. 2007)($ONOO^-$) have been shown to damage cells under culture conditions. In these instances, the supposed mechanism for cell death is mitochondrial damage imparted by unchecked reactive oxygen species, such as superoxide (Murphy 2009). Damage to mitochondria by such species is the suspect of many human maladies, including aging, neurodegenerative disorders, and diabetes (Wallace 2005).

Many important aspects of neural function are mediated by local signals that impinge on only one part of the cell. For example, growth cones at the tips of axons are sensitive to directional cues provided by gradients of chemoattractants and chemorepellants, which guide the axons to their targets (Oliva et al. 2003). Axons are also susceptible to local damage, a common cause of neurodegeneration. Axons are subject to mechanical damage following an injury or by local chemical insults, as lesions that occur in neuroinflammatory diseases like multiple sclerosis. Our chambers provide a means to mimic local signaling *in vitro*.

Several culture systems have been used to tackle seeding-stimulation-response problems to observe axonal transport deficiencies and highlight the root cause of cell damage and death. Neurons are typically studied *in vitro*, as *in vivo* studies are difficult, involving access and stimulation of a live animal. *In vitro* neurobiological studies of multi-cell systems have historically been implemented on bare or modified culture dishes and coverslips. Although a lab standard, coverslips (Kaech and Banker 2006) do not segregate soma and axon and they cannot clearly delineate axonal ownership or polarity. Culture systems using a modified petri dish, Campenot chambers (Campenot 1977, 1982a, b), improve upon coverslips by providing for multi-chamber (typically three-chamber) segregation of neural cells, which are grown in collagen grooves. The chambers are formed by a teflon divider and sealed to the collagen surface with silicone grease. These chambers are prone to leaks, and the dimension of the smallest chamber is approximately 1 mm, limiting the degree to which the solute is localized.

Recently, microfabrication techniques have been implemented to segregate or deterministically order neural cells in predetermined configurations for analysis. Steric approaches dominate in their ubiquity and simplicity: cells are ordered by providing narrow channels though which axons propagate. Generally, channel size and geometry (Lacour et al. 2008; Peyrin et al. 2011) are chosen to permit access and passage to the protruding axon but block migration of cell soma. Once within these channels, the cells can be directed to a second compartment and exposed to a solute, subjected to a gradient within the channel, or both. A popular and influential culture device exploiting this approach is that constructed by Taylor et al. (2003, 2005). This ladder-type device consists of two chambers separated by an array of microchannels shaped to permit axons to grow from the seeding (or somal) chamber to a second (axonal) chamber. By controlling the fluid height between axonal and somal chambers, a hydrostatic head is generated to drive flow from the somal to axonal chambers, and vice versa. By adding a solute to the axonal reservoir, flow induced by the hydrostatic head acts counter to diffusion, establishing a stable, distally directed gradient. The system built by Peyrin et al. (2011) uses similar geometry to generate oriented neural networks for studying neural disease. Kunze et al. (2011) generated opposing groups of soma across microfludically shaped hydrogel compartments, permitting neurite growth and interaction within the hydrogel comparement. Both of these approaches also permit fluid segregation similar to the Taylor et al. approach. To create more complicated solute gradients, Wang et al. (2008) combined laminar flow patterning and neuron culture. Establishing strong gradients required high rates of flow, generating large mechanical shear at the cell-fluid boundary. For their turning assay, Wang et al. shelter the neurons in grooves to mitigate damage to sensitive cellular components. This gradient generator provides for controlled solute profiles both spatially and temporally, but, as the authors are interested in the response of the cell growth cone to stimuli, arrays of neurons are not generated in which axons are separated from soma.

Other approaches, such as photolithographic and microcontact printing (μCP) methods are also used in which a surface is prepared such that cells exhibit a preference for patterned or unpatterned regions of the culture substrate. The photolithographic approach (Kleinfeld et al. 1988) 1980s predates the contemporary microtechniques for cell culture, with the drawbacks that harsh chemicals are used in the preparation of the pattern (photoresist and photoresist solvent), photolithographic tools are required to produce each

device, and it is difficult to increase patterns in complexity. In contrast, microcontact printing (Xia and Whitesides 1998) generates devices from the same microcontact 'stamp', the 'ink' is generally aqueous and non-cytotoxic, and many patterns can be overlayed as the chemistry permits. The primary difficulties in forming μCP patterns stem from chemical and physical affinities between the material to be attached and the surface (e.g., keeping chemistry wet (Oliva et al. 2003)), and the alignment of overlayed patterns (James et al. 2000). μCP patterns effectively guide axons, but intial placement of soma is generally at random, requiring additional structures to block or promote adhesion on the pattern as desired.

Many reviews summarize cell culture methods relevant to neurobiological systems. Banker and Goslin (1998) have described a useful collection of traditional culture methods and procedures, including a discussion of early lithographic patterning approaches and the Campenot chamber. More recent reviews on general microfluidic cell culture systems have been conducted by Meyvantsson and Beebe (2008), as well as Keenan and Folch (2008) with the latter stressing the role of biomolecular gradients. Both works are aimed at general problems in cell biology. Addressing the problem of neural culture, Gross et al. (2007) and Wang et al. (2009) provide reviews on recent work combining microfluidics and neural culture.

In general, neural microfluidic culture systems with solute delivery fall within two broad categories: cells within channels or gels, and cells on a surface. Neurons within channel- and gel-type systems are subjected to chemicals acting at either the distal or proximal end, with a gradient in between and fairly low shear stresses. In surface-type systems, cells are typically probed with a laminar-flow patterning type gradient generator which produces rather large shear stresses transverse to the neuron. The modeling of both these systems is generally straightforward, as cells in both systems are exposed to steady, uniform flows with large Peclet numbers, and diffusion can be ignored. Variations in geometry introduce modeling difficulties, and can be analyzed with finite element techniques (Wang et al. 2008).

Here, we present the design, development, and culture results of a microfluidic device to deliver solutes to rat hippocampal neurons with spatial and temporal resolution. We begin with a discussion of the device design, including its principle of operation, layout, selection of parameters, and design specifications. The design presentation is followed by a procedure for device fabrication and demonstrations of stable cell culture within the constructed device. We close with

conclusions drawn from the design, as well as implications of our design for future neuron studies.

2 Device design

Our design consists of two layers: an upper fluid delivery layer, and a lower culture and growth layer for the cells, as shown in Fig. 1. The top, delivery layer consists of three fluid channels, each connected to a unique inlet reservoir, and a common outlet. A culture layer for cell attachment and directed cell growth sits below this delivery layer. This bottom layer holds an array of axonal channels, vertically offset and perpendicular to the fluid delivery channels, with mismatched hydraulic resistance to confine the delivered solute. Cells are introduced to the culture layer by holes cut through the delivery layer.

This design has several advantages. The footprint of the device is small ($\sim$15 mm^2), reducing required volumes of reagents and cells, but is still easy to manipulate without specialized equipment. Because neurons attach to the bottom surface of the device, growth and transport are easily visualized with an inverted microscope. Actuation by hydrostatic head obviates syringe pumps and tubing; perfusion and solute delivery
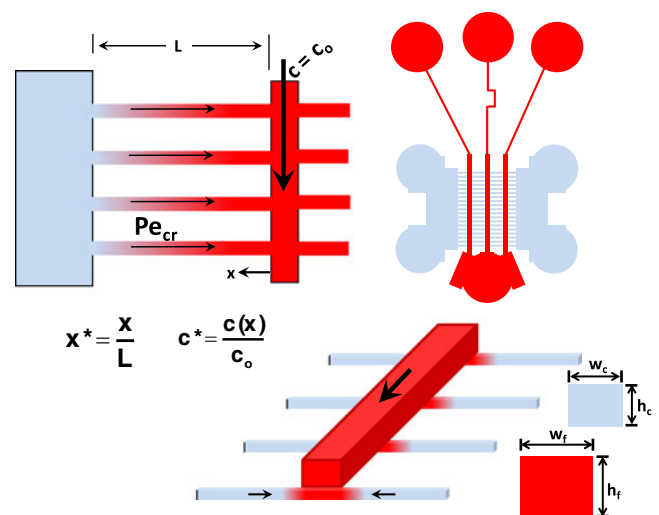
Fig. 1 Various schematics of the device showing relevant features to specify momentum and mass transfer. *Top right:* The layout of the device in two tones. The fluid delivery layer is shown in *red* (*dark*), and the culture layer is shown in *blue* (*light*). *Bottom right:* A demonstration of the operating mechanism. Fluid flows easily through low-resistance channels and is retarded in high-resistance channels. *Arrows* denote directions of flow. *Left:* A dissected view of the device describing variables explained in the text

is prompted by pipetting of reagents/media into one of the seven open reservoirs.

The intersection of the large fluid delivery channels in the upper layer and the small axonal channels in the lower culture layer is important. The axonal channels function by allowing the axon to enter and preventing the passage of the cell soma. We confine solutes from the fluid delivery channels to segments of the axonal channels, through a mismatch of the hydraulic resistances in both the delivery and axonal channels. At the intersection of a large delivery and small axonal channel, mass and momentum are easily transferred across the large delivery channel, but the small axonal channel, exhibiting a much larger hydraulic resistance, retards streamwise convection of fluid from the large channel. By controlling the direction and magnitude of flow in this fluid network, solutes can be confined to segments of the axon.

For a steady, laminar flow, the pressure drop and flow along a channel of uniform geometry are related linearly by a hydraulic resistance:

$$\Delta P = R_h Q \tag{1}$$

Where ΔP is the pressure drop, Q the flowrate, and R_h the resistance along the channel. The resistance may be estimated for rectilinear channels (Kirby 2011) by:

$$R_h = 8\eta \ell \frac{(h+w)^2}{h^3 w^3} \tag{2}$$

Here, η is the viscosity of the fluid, and h, w, and ℓ represent the height, width and length of the channel. For nearly square channels, the resistance scales as $R_h \sim 1/h^4$, giving $Q \sim h^4 \Delta P$ where the flow is strongly nonlinear in the characteristic size of the channel, and linear in the pressure difference. The mathematical stiffness of the flow in response to channel dimension communicates a flow that varies drastically between large and small channels, and a comparatively weak dependence on the pressure difference relegates pressure to a minor role. Therefore, flows will vary strongly between large and small channels, so long as the *differential in pressure drop* between the channels remains small relative to $\frac{h_{\text{large.}}}{h_{\text{small}}}$.

We determine pressure in the device by solving a system of equations relating the pressure drop, flowrate, and hydraulic resistance, as well as continuity of mass at each fluid node in the device ($\sum_{\text{nodes}} Q = 0$). A schematic of the hydraulic resistance model of the system is given in Fig. 2. In this model, each channel has a hydraulic resistance given by Eq. 2. For a device with n axonal channels, there are $7n + 3$ unknown flows within the device. To solve this system, we write $3n$ equations
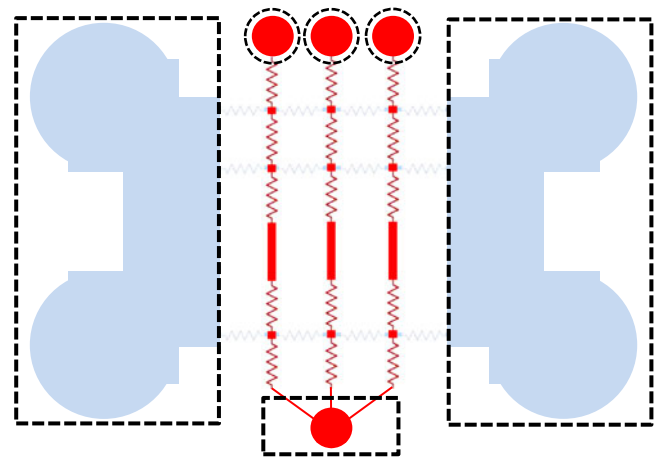
Fig. 2 Device layout recast as a network of hydraulic resistances (resistors) and fixed pressure zones (outlined by *dashed lines*)

enforcing continuity of mass at each node, and $4n + 3$ pressure drop equations of the form $\Delta P = R_h Q$. These pressure-drop equations represent closed fluid circuits (where $\Delta P = 0$), and open-ended circuits incorporating the boundary conditions (here, outlet reservoirs) as endpoints. This system of equations is then solved in MATLAB. The solution yields pressures at each node and flowrates in each channel. This equivalent hydraulic resistance model alone does not predict spatial variation of flow within each channel, and flow velocities are not predicted as a function of position on the channel cross-section; however, the pressure drops combined with later predictions facilitate the three-dimensional velocity distribution far from nodes (i.e., $\ell >> d$ from node).

Mass transfer within the device is well approximated by the one-dimensional convection diffusion equation. This approximation requires that transport along the channel occur at a time scale much greater than similar processes across the channel: $\tau_\parallel >> \tau_\perp$. The ratio of the dominant lengthwise ($\tau_\parallel$) to transverse ($\tau_\perp$) transport time scales in the low axial Pe limit , $\frac{\tau_\parallel}{\tau_\perp} \sim \left(\frac{\ell}{a}\right)^2$, as well as the high axial Pe limit, $\frac{\tau_\parallel}{\tau_\perp} \sim \left(\frac{\ell}{a}\right)^2 \frac{1}{\text{Pe}}$, show that flow within microchannels of moderate Péclet number satisfy the approximation. Thus,

$$\frac{\partial c}{\partial t} + u_x \frac{\partial c}{\partial x} = D \frac{\partial^2 c}{\partial x^2} \tag{3}$$

Where $c(x,t)$ is the local concentration of solute [a.u.], t is time in [s], x the distance along the channel ($0 < x < \ell$) in [m], and D the diffusivity of solute in [m²/s].

We solve Eq. 3 in segmented lengths of the axonal channels. We impose fixed concentration boundary conditions at the intersections between axonal and

delivery channels, $c(0, t) = c_o$, representing the solute imposed on the cell, and a zero-concentration boundary condition where the axonal channels meet the somal chamber, $c(\ell, t) = 0$. We non-dimensionalize Eq. 2 using scaling defined in Fig. 1 and a convective temporal scale to non-dimensionalize time $t^* = \frac{t}{\ell/\bar{u}}$. The velocity scale in this case is the average across the channel, $\bar{u} = \frac{Q}{A}$, computed from knowledge of the device geometry (cross-sectional area, A) and the flowrate from Eq. 1. With this scaling, and noting that $u_x = \bar{u}$ for unidirectional flows, the equation becomes:

$$\frac{\partial c^*}{\partial t^*} + \frac{\partial c^*}{\partial x^*} = \frac{1}{\mathrm{Pe}} \frac{\partial^2 c^*}{\partial x^{*2}} \tag{4}$$

The Péclet number, $\mathrm{Pe} = \frac{\bar{u}\ell}{D} = \frac{\tau_{\mathrm{Diff}}}{\tau_{\mathrm{Conv}}}$, relates the timescales of convection and diffuson along the channel. Often, flows in microdevices have large Péclet numbers, limiting mixing (e.g., laminar flow patterning). Here, a large streamwise Péclet number will similarly result in strong solute confinement, whereas a flow with a near-zero streamwise Péclet number yields a linear concentration profile in the steady-state.

This problem is closed by writing a homogeneous initial condition: $c^*(x^*, 0) = 0$. We perform an eigenfunction expansion to obtain a series solution of this boundary-value problem applicable for all non-zero values of Pe:

$$c^*(x^*, t^*) = e^{\frac{Pe}{2}x^*} \sum_{n=1}^{\infty} \frac{2n\pi}{n^2\pi^2 + 1/4Pe^2} \sin(n\pi x^*)\left(1 - e^{-\frac{t^*}{\tau_n^*}}\right)$$

$$\tag{5}$$

with $\tau_n^* = \frac{1}{\frac{n^2\pi^2}{Pe} + \frac{Pe}{4}}$. For an arbitrary intial solution concentration profile, $\phi(x)$, and zero concentration boundary conditions, the concentration evolves in time and space as:

$$c^*(x^*, t^*) = e^{\frac{Pe}{2}x^*} \sum_{n=1}^{\infty} C_n^* \sin(n\pi x^*) e^{-\frac{t^*}{\tau_n^*}} \tag{6}$$

With the intial-condition-dependent constants:

$$C_n^* = 2 \int_0^1 \phi(x^*) \sin(n\pi x^*) e^{-\frac{Pe}{2}x^*} \, dx^* \tag{7}$$

The Péclet number governs the shape of the concentration profile, both at steady and transient states. The nature of the series solution necessarily means that there is not one single time constant, but a time constant for each mode of the solution. The time constant controlling the development of a concentration profile corresponds to the largest time constant, which is the

lowest Fourier mode, $\tau_1^* = \frac{4Pe}{4\pi^2 + Pe^2}$ or $\tau_1 = \frac{4\ell^2}{D(4\pi^2 + Pe^2)}$; for D = 1e − 9, τ = 2.7 [s], D = 1e − 11, τ = 275 [s].

The shear at the interface between the wall and fluid is determined by solving the steady, 2-D Navier–Stokes equation for uniform flow in a rectangular duct under the action of a pressure gradient $\nabla p = \frac{p_{\mathrm{high}} - p_{\mathrm{low}}}{0 - \ell}$:

$$\nabla p = \eta \nabla^2 u_x = \frac{\partial p}{\partial x} = \eta \left(\frac{\partial^2 u_x}{\partial y^2} + \frac{\partial^2 u_x}{\partial z^2} \right) \tag{8}$$

This is solved in a rectangular domain: $-\frac{w}{2} \leq z \leq \frac{w}{2}$, $-\frac{h}{2} \leq y \leq \frac{h}{2}$, $w > h$ with $u_z = 0$ on the boundary. The velocity profile is given by:

$$u(y, z) = \frac{G\left(\frac{h^2}{4} - y^2\right)}{2\mu}$$
$$- \sum_{\substack{n \\ (\mathrm{odd})}} \frac{4h^2 G}{n^3\pi^3\mu} \sin\left(\frac{n\pi}{2}\right) \cos(\lambda_n y) \frac{\cosh(\lambda_n z)}{\cosh\left(\lambda_n \frac{w}{2}\right)} \tag{9}$$

with $\lambda_n = \frac{n\pi}{h}$ and $G = -\nabla p$. The fluid shear is, in general, a second-order tensor, but the positions of maximal shear reside on the centers of the channel edges. Thus, to identify an upper limit for shear, we need only compute the shear at two points in the domain:

$$\tau_1 = \eta \left. \frac{\partial u}{\partial z} \right|_{z = \pm w/2, \, y = 0}$$
$$= \sum_{\substack{n \\ (\mathrm{odd})}} \frac{4h^2 G}{n^3\pi^3} \lambda_n \sin\left(\frac{n\pi}{2}\right) \tanh\left(\lambda_n \frac{w}{2}\right) \tag{10}$$

$$\tau_2 = \eta \left. \frac{\partial u}{\partial y} \right|_{z = 0, \, y = \pm h/2}$$
$$= -G\frac{h}{2} + \sum_{\substack{n \\ (\mathrm{odd})}} \frac{4h^2 G}{n^3\pi^3} \frac{\lambda_n}{\cosh\left(\lambda_n \frac{w}{2}\right)} \tag{11}$$

Of these, τ_2 is the dominant stress. High shear is present in regions with high fluid velocity gradients, and this is the case on the boundaries of the device; the rectilinear shape of the channel creates points of high shear on the long sides of the channel, as the maximum velocity in the center of the channel must decay to the no-slip value at the wall over a shorter length, increasing the spatial gradient of velocity.

In addition to interfacial stresses, the velocity solution is integrated to give a flowrate, and average velocity:

$$\bar{u} = \frac{Q}{A} = h^2 \frac{G}{4\eta} \left(\frac{1}{3} - \sum_{\substack{n \\ (\mathrm{odd})}} \frac{64}{n^5\pi^5} \frac{h}{w} \tanh\left(\frac{n\pi}{2}\frac{w}{h}\right) \right) \tag{12}$$

Table 1 Geometric parameters tabulated for particular channel aspect ratios

$\dfrac{h}{w}$	ε	δ
1/2	.6303	3.232
1/4	.8144	1.320
1/6	.8763	0.828
1/10	.9258	0.475

The parameters were computed from ca. 1000 summands, at which point the sum had converged

For $w/h > 2$, the hyperbolic tangent is approximated as unity for all n, and the remaining sum, $\sum_{n \,(\text{odd})} \frac{1}{n^5}$ can also be approximated as one. Whence,

$$\bar{u} = h^2 \frac{G}{4\eta} \left(\frac{1}{3} - \frac{64}{\pi^5} \frac{h}{w} \right) \tag{13}$$

We perform a similar procedure to convert the shear stress from an exact transcendental to an approximate algebraic function. In this case, the hyperbolic function does not approach a convenient limit, so we introduce a parameter (Table 1), ε, that depends on the ratio of height to width in the device:

$$\tau_2 = -G \frac{h}{2} \left(1 - \sum_{\substack{n \\ (\text{odd})}} \frac{8}{n^2 \pi^2} \frac{1}{\cosh\left(\frac{n\pi}{2} \frac{w}{h}\right)} \right) = -G \frac{h}{2} (1 - \varepsilon) \tag{14}$$

The above expressions 12 and 13 can be combined to eliminate explicit dependence on pressure, providing a dependence on average velocity in the channel:

$$\tau_2 = \frac{\eta \bar{u}}{h} \left(2 \frac{1 - \varepsilon}{1/3 - \frac{64}{\pi^5} \frac{h}{w}} \right) = \frac{\eta \bar{u}}{h} \delta = \frac{\eta \text{Pe} \frac{D}{\ell}}{h} \delta \tag{15}$$

Equation 15 is convenient to quickly estimate the shear as a function of key geometric and fluid parameters. In keeping theme with the mass convection-diffusion analysis of the system, we find it convenient to recast the shear as a function of Péclet number rather than velocity. We tolerate this addition of variables by noting that the diffusivity of species does not change greatly (if interested in only small ions, $D \sim 10^{-9}$ [m^2/s], or only large macromolecules, $D \sim 10^{-11}$ [m^2/s]), and that the length of the device, although it may change, is typically fixed by the demands of the experiment.

From the solutions to mass and momentum transfer relations, we determine the maximal shear stresses and concentration profiles (in time and space) using the hydraulic resistance model of the device from which the pressure drops were obtained. These results do not require multiphysics modeling of mass and momentum transport, and this is a direct result of design decisions enabling simplifications in the governing equations to analytically tractable forms.

3 Design analysis and discussion

The critical performance and design parameter in the device is the Péclet number, which we have identified as the controlling parameter in the distribution of solutes imposed on the neuron. Below (Fig. 3), we present six plots detailing the concentration of a solute, as normalized by its input concentration, at positions along the culture channels. Solute concentration at six positions (identified by x^*) along the axonal channel are queried as a function of the Péclet number and time and plotted. By selecting a desired channel location and a fraction of the input concentration, the plots yield the Péclet number required for the desired solute profile for transient and steady-state modes of operation.

These concentration isocontours show that the system equilibrates on the order of ten seconds. For most profiles shown, a time of two minutes is sufficient to achieve steady-state operation. These concentration profiles establish more rapidly than standard solute delivery experiments, which are typically over 15 min in duration.

We quantify changes of fluid height analytically with the 1D model presented previously (Eq. 6). This result is necessary to determine the time required to clear an axonal channel at the conclusion of solute injection, for example. To model device clearing, we introduce a nonzero initial condition for the concentration distribution in the channel, along with homogenous boundary conditions on the edges of the channel. By solving a change in device state from an experiment run at $Pe = 15$ with soluble chemicals (i.e., the delivery state) to a cleared device, we have found a 5-fold (e.g., 10^5) reduction in maximum concentration is achieved 4τ after the system is changed from the delivery to the clearing state. This is visualized in Fig. 4, where concentration is shown as a function of time and space, decaying from an initial condition. Here, the time constant is taken as that of the lowest Fourier mode, $\tau = \frac{4Pe}{Pe^2 + 4n^2\pi^2}$.

Our design specifies the Péclet number required such that diffusion is entirely dominated by convection of the fluid from the somal chamber toward the delivery fluidics. Solute confinement is produced at the cost of fluid shear stresses that are imposed along the axon. Fluid shear within the device, as a function of fluid, solute, and geometric parameters, is presented

Fig. 3 Concentration isocontours as a function of time and Péclet number for various positions along the axonal channel (x*)
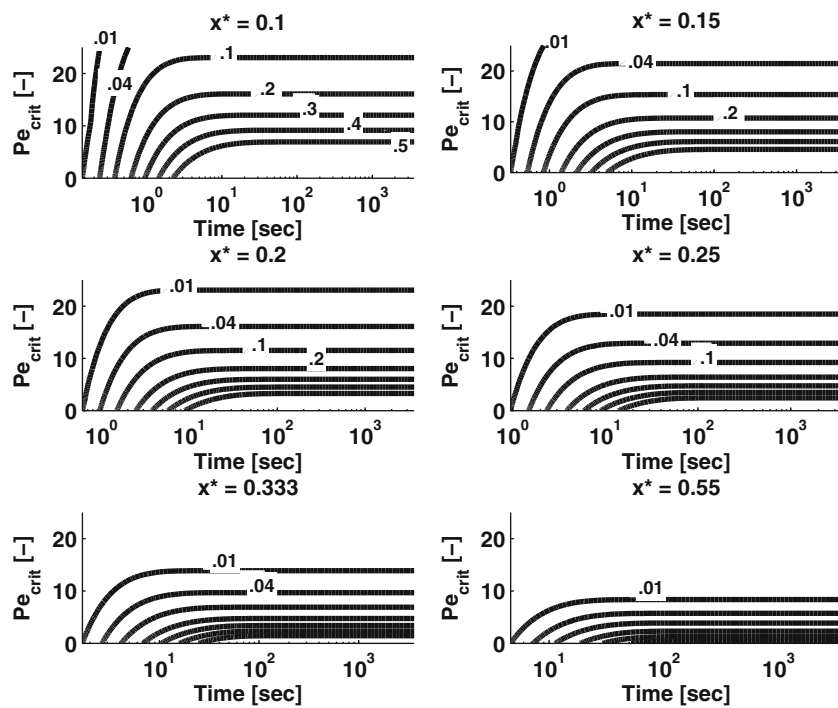
in Eq. 15, and is plotted in Fig. 5. We present two scalings of the shear to highlight important design considerations: (1) allowable channel dimensions for specific values of $\frac{\tau}{Pe}$ under the action of a constant fluid velocity (pressure and resistance changing) and (2) allowable channel dimensions for specific values of $\frac{\tau}{G}$ under the action of a constant pressure difference (flow and resistance changing). Of course, these figures

will collapse to a single curve with appropriate scaling ($\frac{\tau}{Gh}$), and this is shown as an inset in the figure.

The left pane in Fig. 5 shows shear normalized by Péclet number to communicate dependence on the ratio of the channel sides, as well as the absolute height of the channel. Normalization by Péclet removes pressure dependence as the geometry is varied; changes in the shear are due purely to dissipation of energy at the

Fig. 4 Transient response of device from steady-state operation with non-zero boundary conditions to solute clearing state with zero concentration boundary conditions at both ends of the culture channel
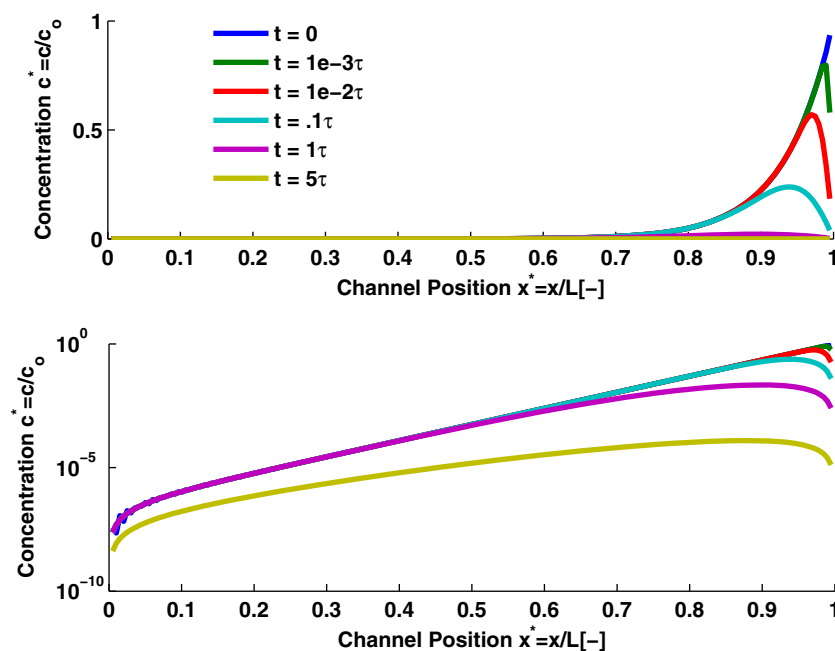
Fig. 5 Maximum shear in the device, normalized by Péclet number (*left*) and pressure gradient (*right*), as a function of absolute channel height and channel aspect ratio. Dimensional quantities are plotted for simplicity in device design. The inset (at *right*) provides the collapsed curves for shear when appropriately normalized
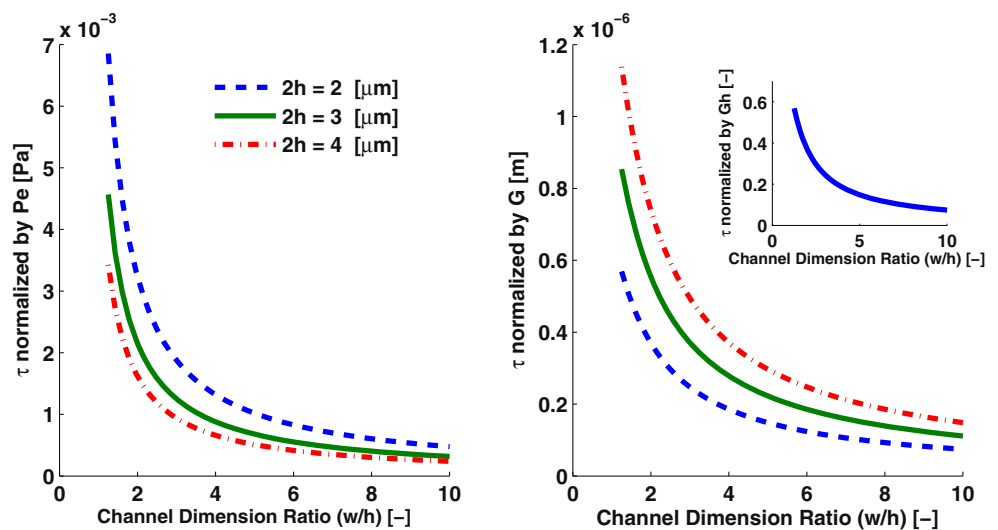
walls vs. dissipation in the bulk—as the channel area is reduced and the cross-section made more oblong, the surface area becomes exaggerated and energy dissipation at the boundaries is enhanced.

At fixed Péclet number, increasing w/h, the channel dimension ratio, and the absolute channel height, h, reduce shear but these parameters are limited by engineering constraints. There are fundamental limitations to the selection of both of these design dimensions, typically imposed by the method of device construction. Dry chemical etching of glass is impractical for depths greater than 3 μm as impurities deposit in the channel halting the etch (in these cases, the glass has a frosty appearance). Wet etching generates channels of arbitrary depth, but semi-circular channels of poor geometric definition. Aside from fabrication constraints, channels with large widths invalidate the arguments used previously to justify a 1-D solute transport model, as enhancement of the channel cross-section decreases $\tau_\perp$ while $\tau_\parallel$ remains constant.

The presence of axons within the channels perturbs channel geometry. Blockage of the channel by cellular components increases the resistance of the channel, decreasing the average fluid velocity in the presence of a constant pressure drop. The pressure drop can be assumed constant as pressure on the somal side is fixed by the culture reservoir height, and the pressure distal from the soma is fixed by the pressure in the fluidic channel which, owing to the small resistance of this channel, is essentially that of the outlet reservoir located at the bottom of the device. We plot shear normalized by the pressure gradient in the culture channel in the right pane of Fig. 5. Here, a blockage is easily seen as a change in both the aspect ratio of the channel as well as the absolute height of the channel. For growth

along the base of the channel, the aspect ratio will increase and the channel height will decrease. Both these effects decrease the incumbent fluid shear on the cells. For growth along the sidewall of the channel, the height remains constant and the shear increasing solely in response to the change in aspect ratio. Since the plot is nonlinear, stronger changes in fluid shear are felt for channels designed with smaller aspect ratios.

Both of these presentations of shear in the device discuss the case of maximal shear occurring a the center of the long wall on the channel cross-section. Locations away from this point will experience lower shear, with a minimum value of zero at the corners of the rectangular cross section.

4 Device fabrication

The two-layer device is constructed from PDMS (for the fluid delivery network) and fused silica (for the culture and growth substrate). PDMS casting masters were fabricated from Silicon wafers (500 [μm] thick) using a Bosch etch process. Prior to etching, wafers are cleaned in Pirahna, dehydrated via heating in a hexamethydisilazane atmosphere (YES Vapor Prime Oven), and patterned photolithographically with Megaposit SPR 220–7.0 positive photoresist spun to a thickness of 7 [μm]. The channels with the smallest aspect ratio (1.3 : 1) in the delivery layer are those residing directly above the axonal channels, having dimensions 135 [μm] × 100 [μm] (height × width), and the channels with the largest aspect ratio (8.4 : 1) construct the resistance network, running from the input reservoir to the large fluid delivery channels. Channels in the resistance network are 16 [μm] in width.

After etching the master, we passivate the surface by exposure to a small liquid volume (~ 80 [μL]) of 1H,1H,2H,2H-perfluorooctyltrichlorosilane (Sigma-Aldrich) vacuum for ~ 2 [hr]. PDMS (Sylgard 184, Dow Corning), mixed in a ratio of 10 : 1 (base: curing agent), degassed, is combined with the master, and baked at 60 [C] for 2 [hr] to form the fluidic layer. After removing the PDMS from the mold, intlet, outlet, and culture reservoirs are installed using a biopsy punch. We employ the leaching procedure of Millet et al. (2007) to remove uncrosslinked oligomers from the PDMS matrix, preventing eventual release of these oligomers during cell culture and device operation. Briefly, a series of solvents swell the PDMS increasing the diffusivity of uncrosslinked polymer. We soak the devices in solutions of pentane (36 [hr]), pentane (7 [hr]), xylenes (16 [hr]), xylenes (7 [hr]), 200 proof Ethanol (2 [hr]), 200 proof ethanol (16 [hr]), 200 proof ethanol (7 [hr]), and a final soak in sterile DI water for a minimum of 12 [hr]. After the final sterile DI water exposure, we dry the PDMS under vacuum or in a 60 [C] oven.

The bottom (culture) layer of the device is fabricated from fused silica. Coverslip-thin (170 [μm]), 4-inch fused silica wafers were ordered from Mark Optics, Inc. (Santa Ana, CA). These wafers are washed in concentrated nitric acid, rinsed with DI water and nitrogen spray-dried prior to patterning. We coat the wafers with 70 [nm] of sputtered Chrome, followed by Shipley 1818 photoresist spun at 3000 RPM for 30 s. We then pattern and develop photoresist to generate a masked array of culture channels, guide lines, and the culture base. Exposed Chrome is removed with CR-14 etchant (Transene Company, Inc. Danvers, MA), and the wafer is again rinsed with DI water and dried in nitrogen.

Using the chrome mask, we perform reactive ion etching to create the culture layer of the device. The chrome mask is etched in CHF_3/Ar plasma (Oxford 100, Oxford Instruments) to a depth of 3 [μm]. After transferring the pattern from the Cr mask to the fused-silica, we remove the remaining photoresist and chrome mask, and clean the wafer in DI water. The cleaned and patterned wafer is then diced with a wafer saw, yielding 24 substrates per wafer.

Both device halves are assembled after activation of the bonding surfaces in air plasma (Harrick Plasma, Ithaca, NY; ~30 [W], 200 [mTorr], 90 [s]). By attaching both layers on an inspection microscope, using a small drop of water between the fused silica and PDMS, we delay the onset of the bond to increase working time and improve alignment. Post-alignment, we gently pinch the parts together and wick residual water from the device edges using a KimWipe. To ensure a strong bond, the assembled device is cured overnight in a 60 [C] oven.

We then prime the device with sterile DI water by filling inlet and culture reservoirs, submerging the device in sterile DI water, and exposing the device to slightly negative pressure to remove bubbles trapped within the device (Monahan et al. 2001). After removing all bubbles, we exchange a solution of 1 [g/L] poly-L-lysine in borate buffer in the device to improve adhesion between the neurons and the wetted surfaces of the device. Typically, we perform two exchanges in total with the second 1.5–2 [hr] following the first. After the poly-L-lysine deposition, we again flush sterile DI water through the device. Devices are stored wet until used.

5 Demonstration of cell culture

We perform culture of primary rat hippocampal neurons in the device. These cells are used to study the distribution and trafficking of motor proteins, growth factors, and other biochemical agents. The neurons are sensitive both mechanically and chemically, providing an excellent test platform for our device.

Primary hippocampal cultures were prepared from E18 embryonic rats of either sex as described previously (Banker and Goslin 1998; Kaech and Banker 2006; Kaech et al. 2012). Cells were plated at 250 cells/mm^2 into the poly-L-lysine-treated somal chamber and maintained in cortical astroglia cells-conditioned NB/B27 medium at 37° incubator with 5% CO2. Due to evaporation, medium was replenished every other day. Cells attached to the surface a few hours after seeding and axons started to grow into the micro-channels 3–5 days after seeding. For visualization of neurite growth, 10 [μM] Calcein AM (Invitrogen), a cell-permeant dye that is converted to a green-fluorescent calcein after acetoxymethyl ester hydrolysis by intracellular esterases, was added to the somal chamber for 15 [min] incubation at 37° followed by gentle rinse with pre-warmed medium. To label mitochondria, 50 [nM] MitoTracker® dye (Invitrogen) was added to the somal chamber for 30 [min] incubation at 37° followed by gentle rinse with pre-warmed medium. Cells were maintained at 37° for live imaging. Before acquiring movies, nanochamber was semi-sealed into a heated chamber (Warner instruments, Hamden, CT) containing hibernate A medium (Brainbits LLC, Springfield, IL) kept at 37°. Images were captured with a spinning disk confocal microscope setup custom built by Solamere Technology Group (Salt Lake City, Utah).

Fig. 6 Phase contrast image of cells within device at DIV 1 (*left*) and DIV 7 (*right*). Cells at DIV 7 display healthy morphology evidenced by the absence of clumping and the outgrowth and development of both dendrites and axons. Images were captured on an inverted microscope, enabled by the coverslip-thin device substrate. The scale bar in both figures is 140 [μm]
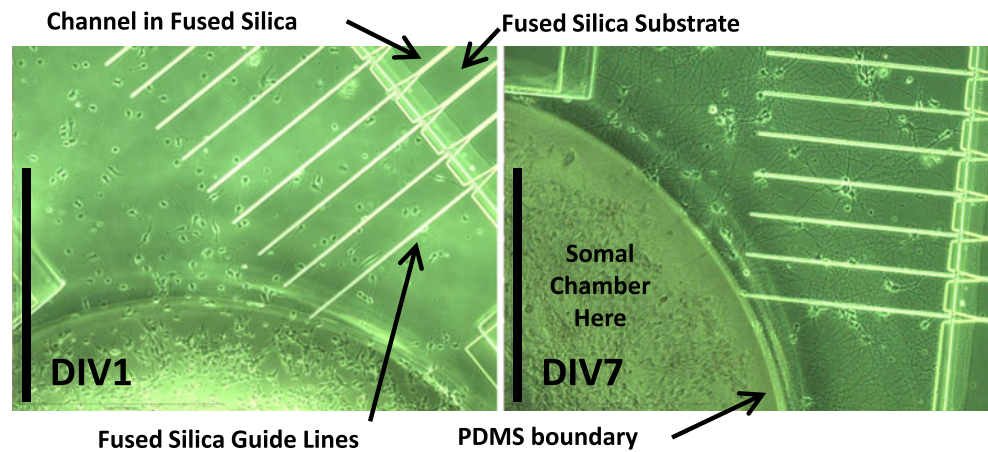
Laser excitation wave length for different fluorophores was 488 [nm] for GFP and 568 nm for Mitotracker Red. Mitochondrial transport was acquired using a 40X 1.3 N.A oil objective. Both objective and the imaging stage are heated to 37°.

We image cells using phase contrast microscopy to gauge cell viability and directed growth. Cells are shown at day *in vitro* (DIV) 1 and DIV 7 in Fig. 6. These images show the growth of cells from a globular to stellated morphology, concurrent with the extension of axons into the culture channels. As described in the previous section, guide lines were fabricated onto the surface of the device where the cells are seeded.

These guide lines are marked in Fig. 6, leading from the seeding area toward the trigonal opening of the culture channels. Neurons were successfully cultured in the closed device up to DIV 11, which is sufficient time for cells to reach fluidic channels within the device enabling confined solute delivery.

We found guide lines into the axonal channel necessary to align the culture channels with the axon of the seeded cells. This observation is, at first glance, inconsistent with the work of Taylor et al. (2003, 2005), as they do not require special modification of the entrance region to their channels. There are, however, geometric differences between our work and Taylor
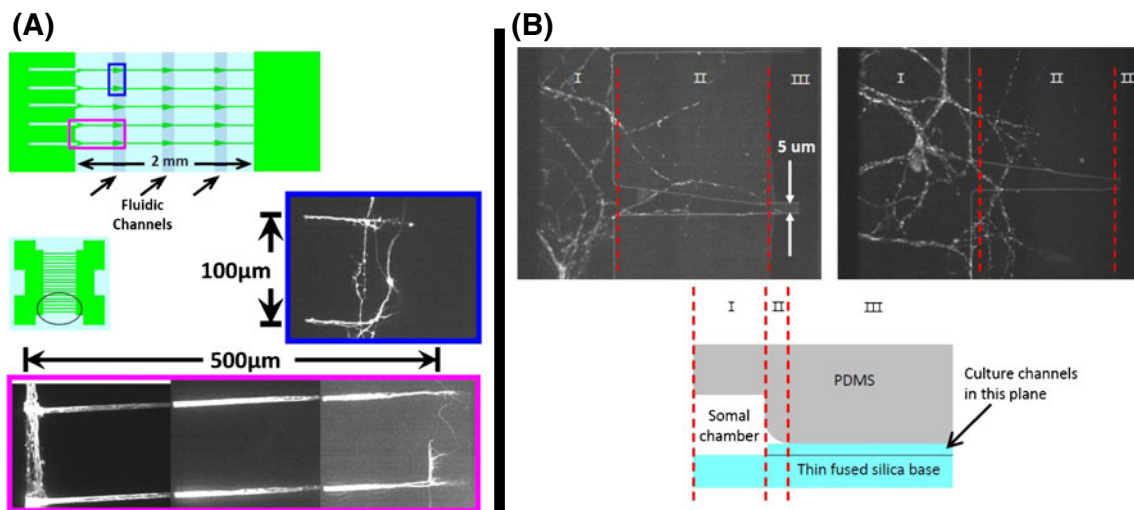
Fig. 7 Frame (**A**) Demonstration of entrained neural axons within culture channels. Fluorescence micrographs (*middle right* and *bottom*), with corresponding device locations highlighted at top, show stained (Calcein AM, Invitrogen) cells indicating the presence of axons within the channels. Growth of axons proceeds from the somal chamber to the first fluidic channel. Frame (**B**) Micrographs (*top*) and diagram (*bottom*) of axons in a device *without* guide lines. In the bottom diagram, three zones are specified: (I) the somal chamber, (II) partially enclosed culture channels, and (III) completely enclosed culture channels. Shown above are micrographs of axons failing to enter the channels in zone (III), having been stalled in zone (II). The micrographs at top were captured using fluoresence microscopy on cells treated with MitoTracker Green dye, visualizing the mitochondria within the cells

et al. which explain the differences in cell behavior. The interface between the small channels and the culture area is formed by the attachment of the top PDMS cover and the bottom fused-silica base. When attached, the PDMS cover and base form a seal above the culture channels which is not entirely flush and the region between the PDMS top and fused silica base presents the cells with a three-dimensional charged surface (the entire device has been coated with cationic poly-lysine) that is amenable to cell growth and attachment. Both the fabrication of the PDMS cover and the alignment of the PDMS/fused-silica assembly contribute to the geometry of this surface. The edges on the PDMS cover are not perpendicular, but curved owing to the etching of the master; off-edge alignment exaggerates the extent of the bounding surface (Fig. 7).

6 Conclusions

We have presented a design methodology quantifying the effects of device geometry on mass transport and fluid shear. These results were used to design a microfluidic device, in which nerve cells were successfully cultured. The design methodology presents a two-step process: (1) a hydraulic resistance model is used to predict fluid flow and pressure drops in all channels within the device (2) the pressure drops and flow rates are used to predict fluid shear and solute distribution profiles. This approach obviates implementation of multiphysics or CFD software, requiring only implementation of a matrix solver—mass transport and momentum behavior are straightforwardly communicated via plots and tables to determine shear as a function of flowrate and geometry, along with transient and steady state solute distributions given previously-determined flow behavior. This reduced-order design formulation enables fast and straightforward design of arrayed microfluidic devices for neural culture.

Culture on the device was demonstrated using primary embryonic rat hippocampal neurons. We also describe a geometric guidance scheme to direct axonal processes of the neurons into a linear array of culture channels where the axons may be later analyzed using the fluidic delivery system. Such a system will be useful in neurobiological experiments such as drug screening for prevention of, or solube factor delivery for the encouragement of, transport defects within the axon. Furthermore, the layout of the device enables somal isolation (and therefore known cell polarity) and the multiplexed culture channels of known orientation permit addressable data collection with minimal effort.

References

G. Banker, K. Goslin (eds.), *Culturing nerve cells* (MIT Press, 1998)

R. B. Campenot, Local Control of Neurite Development by Nerve Growth-Factor. P Nat. Acad. Sci. USA **74**(10), 4516–4519 (1977)

R.B. Campenot, Development of sympathetic neurons in compartmentalized cultures 1. local-control of neurite growth by nerve growth-factor. Dev. Biol. **93**(1), 1–12 (1982a)

R.B. Campenot, Development of sympathetic neurons in compartmentalized cultures 2. local-control of neurite survival by nerve growth-factor. Dev. Biol. **93**(1), 13–21 (1982b)

K.J. De Vos, A.J. Grierson, S. Ackerley, C.C. Miller, Role of axonal transport in neurodegenerative diseases. Annu. Rev. Neurosci. **31**(1), 151–173 (2008)

P.G. Gross, E.P. Kartalov, A. Scherer, L.P. Weiner, Applications of microfluidics for neuronal studies. J. Neurol. Sci. **252**(2), 135–143 (2007)

C. James, R. Davis, M. Meyer, A. Turner, S. Turner, G. Withers, L. Kam, G. Banker, H. Craighead, M. Issacson, J. Turner, W. Shain, Aligned microcontact printing of micrometer-scale poly-l-lysine structures for controlled growth of cultured neurons on planar microelectrode arrays. IEEE Trans. Biomed. Eng. **47**(1), 17–21 (2000)

S. Kaech, G. Banker, Culturing hippocampal neurons. Nat. Protoc. **1**(5), 2406–2415 (2006)

S. Kaech, C.F. Huang, G. Banker, Short-term high-resolution imaging of developing hippocampal neurons in culture. Cold Spring Harb. Protoc. (2012). doi:10.1101/pdb.prot068247

T.M. Keenan, A. Folch, Biomolecular gradients in cell culture systems. Lab Chip **8**, 34–57 (2008)

B.J. Kirby, *Micro- and Nanoscale Fluid Mechanics Transport in Microfluidic Devices* (Cambridge University Press, 2011)

D. Kleinfeld, K. Kahler, P. Hockberger, Controlled outgrowth of dissociated neurons on patterned substrates. J. Neurosci. **8**(11), 4098–4120 (1988)

A. Kunze, R. Meissner, S. Brando, P. Renaud, Co-pathological connected primary neurons in a microfluidic device for alzheimer studies. Biotechnol. Bioeng. **108**(9), 2241–2245 (2011)

S.P. Lacour, R. Atta, J.J. FitzGerald, M. Blamire, E. Tarte, J. Fawcett, Polyimide micro-channel arrays for peripheral nerve regenerative implants. Sens. Actuators, A, Phys. **147**(2), 456–463 (2008)

I. Meyvantsson, D.J. Beebe, Cell culture models in microfluidic systems. Annu. Rev. Anal. Chem. **1**(1), 423–449 (2008)

L.J. Millet, M.E. Stewart, J.V. Sweedler, R.G. Nuzzo, M.U. Gillette, Microfluidic devices for culturing primary mammalian neurons at low densities. Lab Chip **7**, 987–994 (2007)

J. Monahan, A.A. Gewirth, R.G. Nuzzo, A method for filling complex polymeric microfluidic devices and arrays. Anal. Chem. **73**(13), 3193–3197 (2001)

M.P. Murphy, How mitochondria produce reactive oxygen species. Biochem. J. **417**, 1–13 (2009)

A.A. Oliva, C.D. James, C.E. Kingman, H.G. Craighead, G.A. Banker, Patterning axonal guidance molecules using a novel strategy for microcontact printing. Neurochem. Res. **28**, 1639–1648 (2003)

T.M. Pearce, J.C. Williams, Microtechnology: Meet neurobiology. Lab Chip **7**, 30–40 (2007)

J.M. Peyrin, B. Deleglise, L. Saias, M. Vignes, P. Gougis, S. Magnifico, S. Betuing, M. Pietri, J. Caboche, P. Vanhoutte, J.L. Viovy, B. Brugg, Axon diodes for the reconstruction of oriented neuronal networks in microfluidic chambers. Lab on a Chip **11**(21), 3663–3673 (2011)

R.B. Schoch, J. Han, P. Renaud, Transport phenomena in nanofluidics. Rev. Mod. Phys. **80**, 839–883 (2008)

R. Selvatici, M. Previati, S. Marino, L. Marani, S. Falzarano, I. Lanzoni, A. Siniscalchi, Sodium azide induced neuronal damage *in vitro*: evidence for non-apoptotic cell death. Neurochem. Res. **34**, 909–916 (2009)

T.M. Squires, S.R. Quake, Microfluidics: Fluid physics at the nanoliter scale. Rev. Mod. Phys. **77**, 977–1026 (2005)

C. Szabo, H. Ischiropoulos, R. Radi, Peroxynitrite: biochemistry, pathophysiology and development of therapeutics. Nat. Rev., Drug Discov. **6**(8), 662–680 (2007)

A.M. Taylor, M. Blurton-Jones, S.W. Rhee, D.H. Cribbs, C.W. Cotman, N.L. Jeon, A microfluidic culture platform for cns axonal injury, regeneration and transport. Nat. Methods **2**(8), 599–605 (2005)

A.M. Taylor, S.W. Rhee, C.H. Tu, D.H. Cribbs, C.W. Cotman, N.L. Jeon, Microfluidic multicompartment device for neuroscience research. Langmuir **19**(5), 1551–1556 (2003)

D. Wallace, A mitochondrial paradigm of metabolic and degenerative diseases, aging, and cancer: a dawn for evolutionary medicine. Annu. Rev. Genet. **39**, 359–407 (2005)

C.J. Wang, X. Li, B. Lin, S. Shim, G.l. Ming, A. Levchenko, A microfluidics-based turning assay reveals complex growth cone responses to integrated gradients of substrate-bound ecm molecules and diffusible guidance cues. Lab Chip **8**, 227–237 (2008)

J. Wang, L. Ren, L. Li, W. Liu, J. Zhou, W. Yu, D. Tong, S. Chen, Microfluidics: a new cosset for neurobiology. Lab Chip **9**, 644–652 (2009)

Y. Xia, G.M. Whitesides, Soft lithography. Annu. Rev. Mater. Sci. **28**(1), 153–184 (1998)